Twinning-induced plasticity (TWIP) effect in multi-phase metastable beta Zr-Nb alloys

Junhui Tang, Ahmed Zorgati, Jean-Baptiste Gaillard, Philippe Vermaut, Frédéric Prima, Fan Sun

Twinning-induced plasticity (TWIP) effect in multi-phase metastable beta Zr-Nb alloys

(This is the revised version on submission to JMST 07-2022)

Junhui Tang [a], Ahmed Zorgati [b], Jean-Baptiste Gaillard [c], Philippe Vermaut [a, d], Frédéric Prima [a], Fan Sun [a,*],

[a] *PSL Research University, Chimie ParisTech, CNRS-UMR8247, Institut de Recherche de Chimie Paris, Paris, 75005, France*

[b] *Sorbonne University, Ecole Polytechnique, Palaiseau, 91128, France*

[c] *Paris-Saclay University, Commissariat à l'Energie Atomique, Service d'Etude des Matériaux Irradiés, Gif-Sur-Yvette, 911191 France*

[d] *Sorbonne University, UPMC University Paris, UFR926, Paris, 75005, France*

* Corresponding authors.

E-mail address: fan.sun@chimieparistech.psl.eu (F. Sun).

Abstract

The deformation mechanisms were studied in metastable Zr-13.8Nb-0.7Hf and Zr-15.5Nb-0.7Hf (wt.%) alloys exhibiting complex microstructures due to quenched-in precipitates (acicular body-centered tetragonal phase and globular monoclinic phase) in beta grains. Twinning-induced plasticity (TWIP) effect was observed in Zr-13.8Nb-0.7Hf via {332}<113> twinning operation, resulting in higher strain-hardening rate and uniform elongation than those of Zr-15.5Nb-0.7Hf deforming via only dislocation glide. *In-situ* characterizations, by applying tensile deformation during electron backscattered diffraction (EBSD) mapping and transmission electron microscopy (TEM) observation, were conducted to clarify the twinning process and the role of quenched-in precipitates

when interacting with deformation twins.

Key words: Zirconium alloys; Twinning-induced plasticity; Deformation structure; *In-situ* TEM traction; *In-situ* EBSD traction

During the last decades, a large amount of scientific works had been devoted to β-type Zr and Ti alloys for biomedical applications due to their high strength, good corrosion resistance, low magnetic susceptibility and superior biocompatibility [1]. A strategy dedicated to a general improvement of mechanical properties on Ti-based alloys had been achieved by introducing twinning-induced plasticity (TWIP) and transformation-induced plasticity (TRIP) effects via metastability control of the β matrix. Multiple deformation mechanisms, including {332}<113> twinning (332T), {112}<111> twinning (112T), stress-induced martensitic (SIM) transformation (orthorhombic martensite α″) as well as dislocation slip, had been reported to be responsible for the excellent mechanical properties in metastable Ti-based alloys [2-7]. Among them, 332T and SIMα″ had attracted much interest due to their effective improvement of strain-hardening rate, mainly as a result of dynamic Hall-Petch effect, and the subsequent improvement of uniform elongation during tensile plastic flow [3]. In beta metastable Zr alloys, much less information is, so far, available in the literature. As a fact, various twinning modes, such as classical 112T mode [8] and newly observed 332T mode [9-12], were operational in body-centered cubic (BCC) matrix under mechanical loading. Similar band-like products could be obtained in the parent beta Zr grains after the plastic deformation as those in beta Ti alloys. As for TRIP/TWIP Ti alloys, the motivation to improve strength-ductility combination of Zr alloys is driven by safety-critical applications requiring high strain-hardening rate. One of the demands arise from cardiovascular stent applications which highly require a combination of high density (for high X-ray visibility), low magnetic susceptibility (for improved magnetic resonance imaging (MRI) compatibility) and excellent biocompatibility (free of Ni, Cr or Co elements) interestingly fulfilled by Zr alloys [13]. So far, the use of Zr alloys was however hindered by their poor natural strain-hardenability and limited ductility which

might lead to stent fracture due to premature strain-localization during the plastic expansion in coronary artery [14, 15]. As a consequence, introducing TWIP approach to develop new Zr-based strain-transformable alloys is of great interest to enhance the overall strain-hardenability of alloys in the Zr systems.

As a beta stabilizer, Nb was shown to be an effective element used in the design of low-modulus Zr-based alloy to achieve low shear modulus and thermoelastic martensitic transformations. Many studies had been carried on metastable Zr-Nb alloys [8-12, 16-22]. The SIMα″ was confirmed to occur in Zr-Nb-Sn alloys reported by Okabe et al [22], resulting in shape memory effect and superelasticity. Mechanical twinning had been reported in Zr-Nb [8-12], Zr-Mo [23] and Zr-Mo-Al [24] alloys, however, the potential TWIP effect had not been explored yet in metastable beta Zr alloys. Unlike single-phase metastable beta Ti alloys at solution treated state, it has been reported that the Zr-Nb based alloys exhibit several secondary phases, such as body-centered tetragonal (BCT) Widmanstätten phase with a c/a ratio of 1.1 [19, 21] and monoclinic phase [20]. Their interactions with mechanical twinning are still unknown.

In order to study the TWIP effect in Zr alloys, Zr-Nb compositions with and without mechanical twinning were designed according to the critical electron-to-atom ratio (e/a = 4.144) based on Pauling metallic valences. The critical e/a corresponds to Zr-14.6Nb (wt.%), which is the critical Nb concentration above which the beta phase can be fully stabilized [25]. Therefore, the target compositions were set to critical composition +/- 1wt% Nb. By using commercial purity Zr (99.2%) and Nb metals (99.9%), the final ingots obtained by arc melting (five times remelting in a Buhler AM500 furnace) yielded Zr-13.8Nb-0.7Hf (wt.%) (e/a=4.136) and Zr-15.5Nb-0.7Hf (wt.%) (e/a=4.153) according to quantitative micro-analysis (Bruker XFLASH 6/60 Energy Dispersive X-ray (EDX) spectroscopy system).

Raw ingots were annealed in vacuum tubular furnace under 2.0×10^{-4} Pa at 1193 K for 1.8 ks with subsequent water quenching. 0.5 mm thickness sheets were obtained by cold-rolling with a 90% reduction rate for both alloys. Tensile samples with a thickness of 0.5 mm and a gauge section of 10×3 mm^2 were machined from the cold-rolled sheets. The samples were recrystallized at 1193 K under 2.0×10^{-4} Pa for 1.8 ks

then water quenched to retain beta matrix (called ST state hereafter). Uniaxial tensile tests were performed on an INSTRON 5982 machine at room temperature with a constant strain rate of 10^{-3} s^{-1}. Phase characterization was carried out by X-ray diffraction (XRD) using Bruker D8 ADVANCE with CuKα radiation operating at 40 kV and 40 mA. Electron backscattered diffraction (EBSD) mapping was performed using a LEO 1530 FEG-SEM operating at 20 kV with a Nordif high-speed camera. A JEOL 2100plus transmission electron microscope (TEM) operating at 200 kV was used for fine-scale microstructures observations before and after deformation in both alloys. The *in-situ* methods using the same dimensional tensile samples were employed to characterize the twinning behaviors in Zr-13.8Nb-0.7Hf on a Proxima 100-Micromecha machine for EBSD mapping by holding tensile strain at different strain steps with a constant strain rate of 2.0×10^{-3} s^{-1}. For *in-situ* TEM investigation, a GATAN 672 single tilt heating-straining holder was used to observe the twin-BCT interaction. Samples for *in-situ* TEM observations (10 mm × 2 mm × 0.1 mm) were prepared by a twin-jet polishing technique, using a solution of 7% sulfuric acid in methanol, held at about 250 K. Schmid factor (SF) [7] analysis was performed to interpret *in-situ* TEM results.

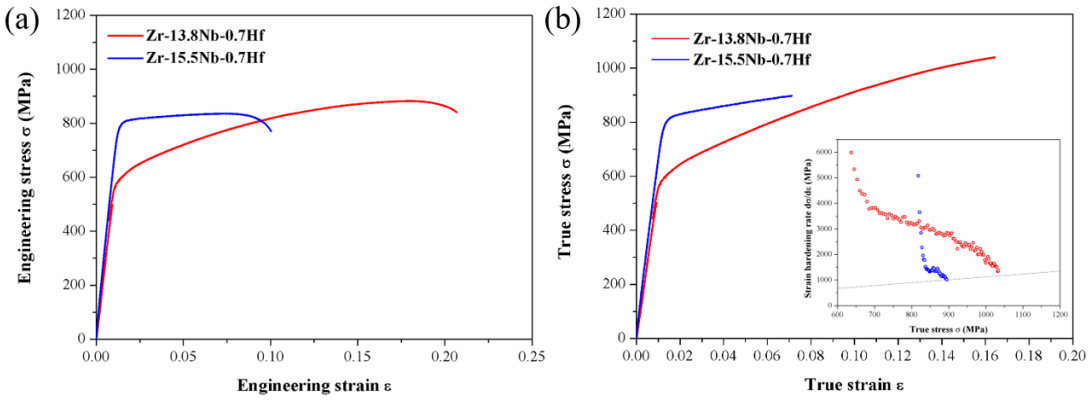

Fig. 1. Mechanical response of Zr-13.8Nb-0.7Hf and Zr-15.5Nb-0.7Hf samples at ST state. (a) Tensile engineering stress-strain curves. (b) True stress – true strain curves, the inset is the corresponding strain-hardening rate curves as a function of true stress.

Fig. 1 displays the mechanical properties of Zr-13.8Nb-0.7Hf and Zr-15.5Nb-0.7Hf alloys at ST state. As observed in Fig. 1a, Zr-15.5Nb-0.7Hf alloy exhibits a higher

yield strength (YS) at ~790 MPa, when compared to Zr-13.8Nb-0.7Hf alloy at ~570 MPa. In contrast, a higher ultimate tensile stress (UTS) was observed in Zr-13.8Nb-0.7Hf (~880 MPa) when compared to Zr-15.5Nb-0.7Hf (~830 MPa), due to an extremely large improvement of the strain-hardening rate in Zr-13.8Nb-0.7Hf, during plastic deformation. The inset of Fig. 1 shows strain-hardening rate evolutions as a function of true stress. The strain-hardening rates of both alloys are observed to decrease from very high rates due to elastic-plastic transition until the formation of the necking where $d\sigma/d\varepsilon = \sigma$ (Considère line shown in dashed line in the inset of Fig.1). The strain-hardening rate of Zr-13.8Nb-0.7Hf alloy stays above the Considère line until ~1040 MPa of true stress, resulting in an average strain hardening rate about 2.7 GPa and a uniform elongation of 0.16. For Zr-15.5Nb-0.7Hf, the true strain-hardening rate decreases rapidly to Considère line at ~900 MPa, showing an average rate about 1.3 GPa and a uniform elongation of 0.07.

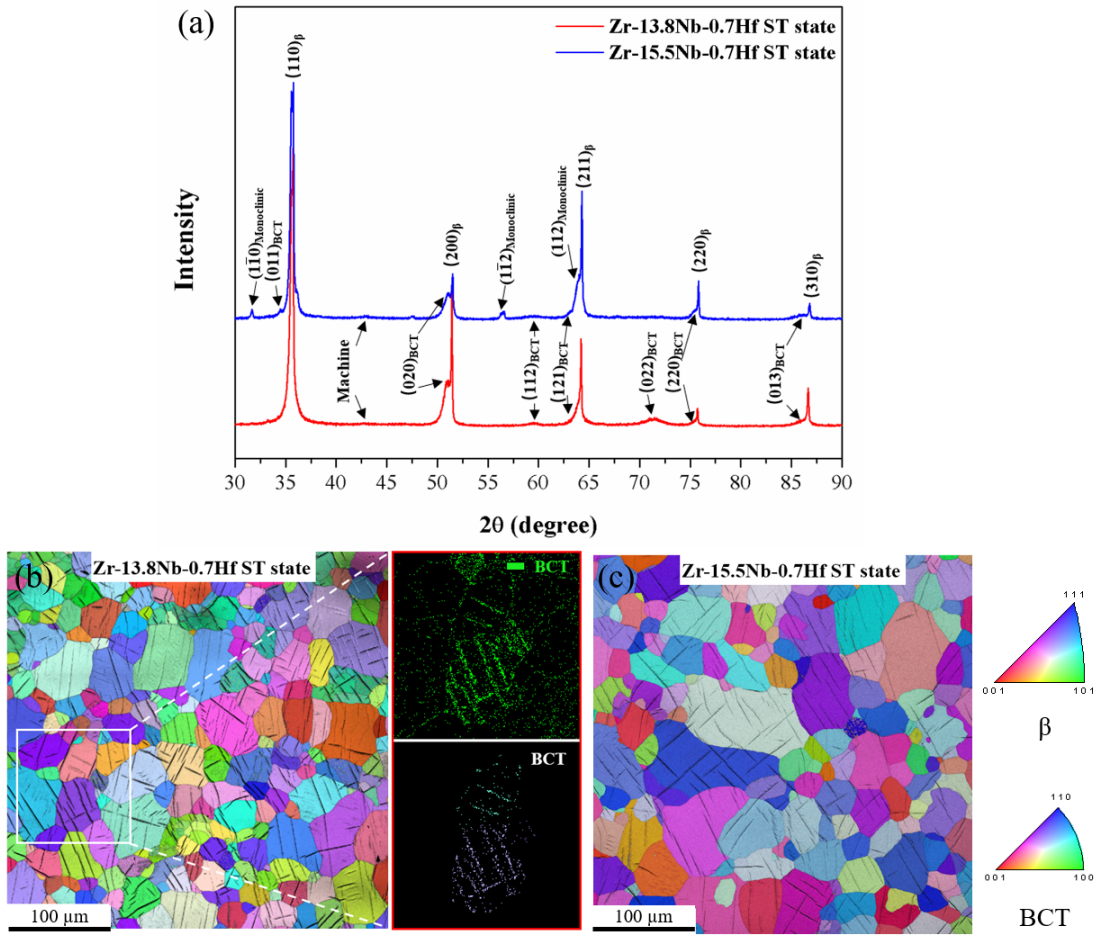

Fig. 2. Microstructural characterization of Zr-13.8Nb-0.7Hf and Zr-15.5Nb-0.7Hf alloy at ST state. (a) XRD profiles; (b) and (c) EBSD maps (image quality-IQ + inverse pole figure-IPF). The phase map and IPF map for BCT phase marked in (b) are given, respectively.

The microstructural analysis of both samples, at ST state, was performed by XRD and EBSD methods. The results are shown in Fig. 2. On the diffractograms, both ST samples show high-intensity peaks corresponding to BCC beta phase (a = 3.551 Å for Zr-13.8Nb-0.7Hf, a = 3.548 Å for Zr-15.5Nb-0.7Hf) and additional peaks due to secondary phases. The identification of the secondary phases detected in both alloys were performed by combining XRD, EBSD and TEM diffraction patterns to cross-check the results. The secondary phase identified in Zr-13.8Nb-0.7Hf is shown to be a body-centered tetragonal (BCT) phase with cell parameter a = b = 3.57 Å, c = 3.92 Å, c/a = 1.10, similar to the values reported in literature [21]. Two secondary phases can be identified in Zr-15.5Nb-0.7Hf, one exhibits similar BCT structure with a = b = 3.57 Å, c = 3.98 Å, c/a = 1.11 and the other is of monoclinic structure which has also been reported in literature [20, 21]. According to the diffractograms, the intensities of the monoclinic peaks in Zr-15.5Nb-0.7Hf are very limited, which could be due to a low volume fraction of such phase in the alloy. Corresponding peaks are indexed in Fig. 2a, the notation “BCT” was used for the BCT phase and “monoclinic” for the monoclinic phase hereafter in the paper.

EBSD maps of the Zr-13.8Nb-0.7Hf and Zr-15.5Nb-0.7Hf alloys at ST state shown in Fig. 2(b, c) display equiaxed recrystallized beta phase. Notable acicular BCT precipitates can be observed in both alloys with a length of about 50 micrometers. The width of the BCT needles was about 100 nm, close to the resolution limit of the EBSD mapping. In some beta grains near [111] orientation, the large BCT precipitates can be identified by EBSD indexation as shown in the magnified phase map in Fig. 2b. However, no monoclinic phase was identified with enough confidence by using the same indexation process. The difficulty was probably raised by the low volume fraction

of the phase which limited the chance to capture large-enough precipitates in a well-oriented beta grain.

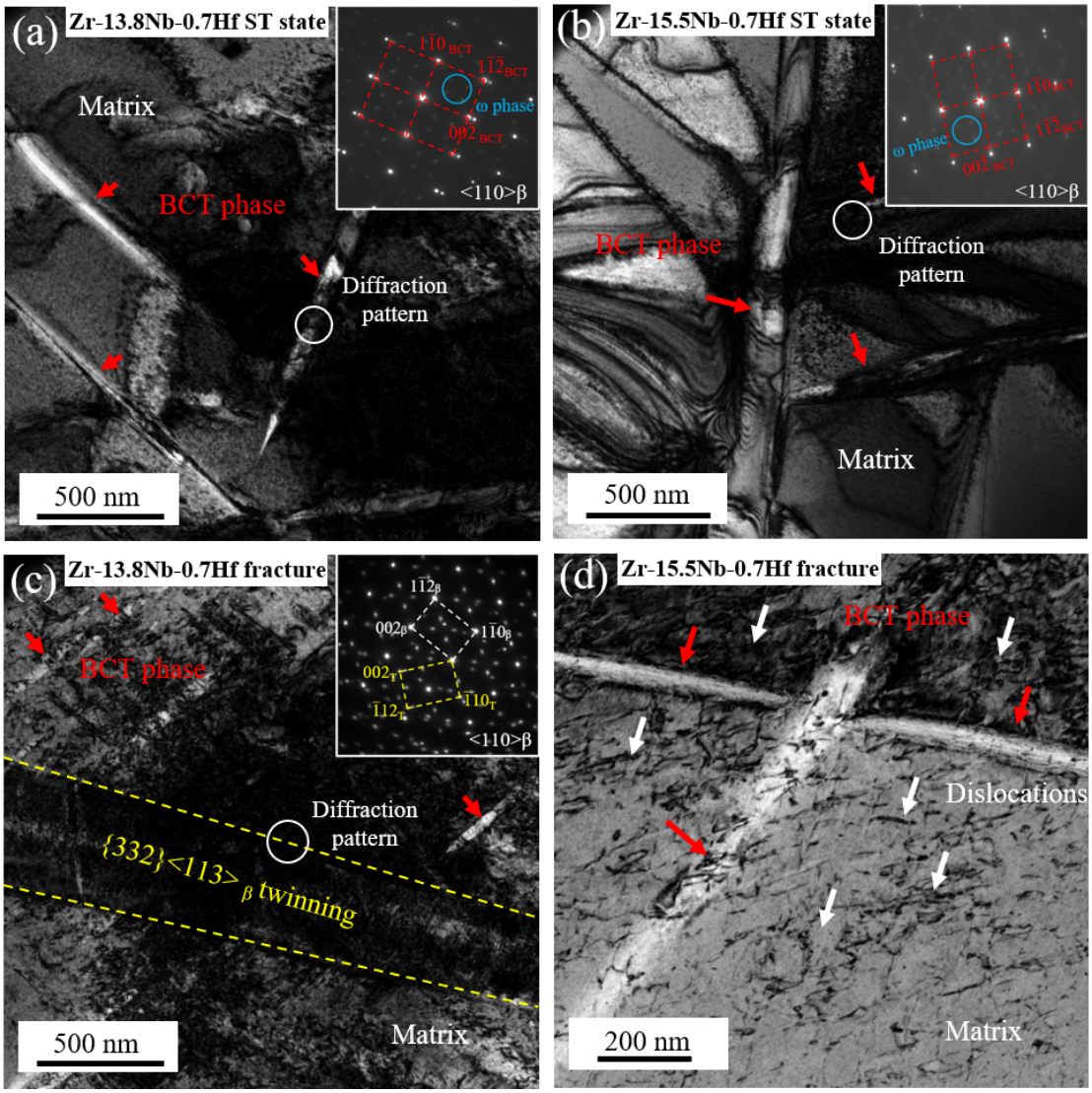

Fig. 3. TEM micrographs of Zr-Nb alloy. (a) and (c) bright-filed (BF) images of Zr-13.8Nb-0.7Hf at ST state and deformed state (until fracture), respectively; (b) and (d) BF images of Zr-15.5Nb-0.7Hf at ST state and deformed state, respectively. Inserts are corresponding SAED patterns marked in the BF images.

Fig. 3 shows the TEM micrographs of the Zr-13.8Nb-0.7Hf and Zr-15.5Nb-0.7Hf alloys before deformation and after fracture, respectively. According to bright filed images Fig. 3(a, b), the acicular BCT phase was observed (red arrows) in both alloys at ST state, consistently with XRD analyses. The selected area electron diffraction (SAED)

patterns recorded along $<110>_{\beta}$ zone axis clearly demonstrates the lattice correspondence between BCT and parent BCC: $[110]_{BCT}$ // $[110]_{\beta}$, $(002)_{BCT}$ // $(002)_{\beta}$, $(1\bar{1}0)_{BCT}$ // $(1\bar{1}0)_{\beta}$; $d_{1\bar{1}0BCT} = d_{1\bar{1}0\beta}$; $d_{002BCT} = 1.1d_{002\beta}$, in both alloys. The reflections at 1/3 and 2/3 $\{112\}_{\beta}$ positions in the SAED pattern of the beta matrix, indicate the presence of athermal omega phase formed during the water-quenching [26].

Fig 3(c, d) exhibits the TEM bright field micrographs of the deformed Zr-13.8Nb-0.7Hf and Zr-15.5Nb-0.7Hf samples after fracture in the tensile test. 332T was observed in Zr-13.8Nb-0.7Hf after tensile deformation (Fig. 3c), the twinning orientation relationship being determined by SAED along $<110>_{\beta}$ zone axis at twin interface (shown in insert of Fig. 3c). In contrast, in bright field TEM image of the Zr-15.5Nb-0.7Hf after tensile test, massive dislocation activity can be observed in beta matrix without presence of any 332T and in BCT phases.

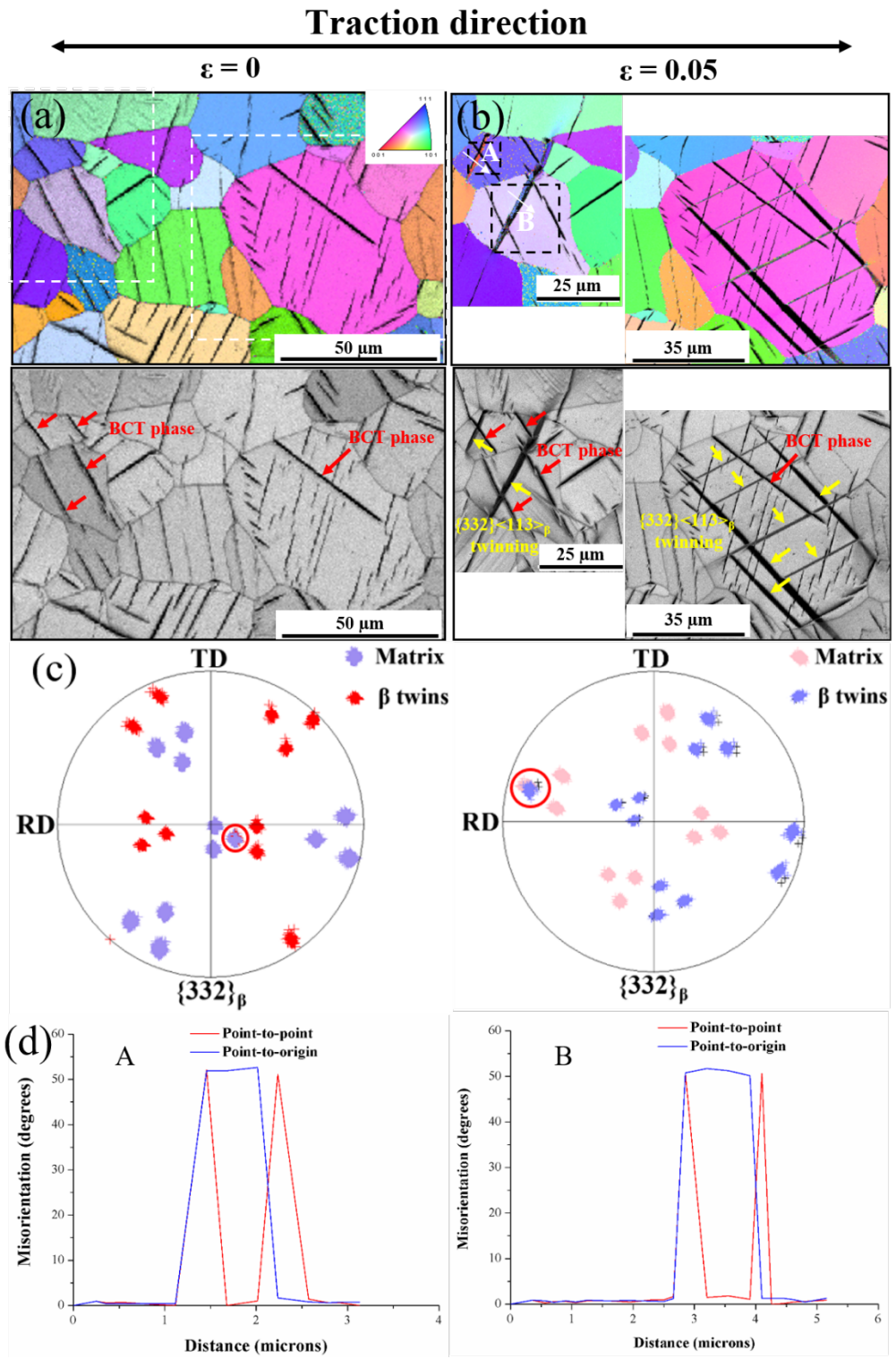

Fig. 4. *In-situ* EBSD mapping of Zr-13.8Nb-0.7Hf alloy during traction taken from the same region (IPF + IQ): (a) strain ε = 0; (b) strain ε = 0.05; (c) pole figures of beta matrix, 332T corresponding to the grains marked in (b). (RD – rolling direction, TD – transverse direction); (d) misorientation profiles along the arrows labelled A and B in (b) as typical examples.

In order to clarify the activation and the evolution of the twinned microstructure of Zr-13.8Nb-0.7Hf alloy, *in-situ* tensile tests were performed in SEM coupled with EBSD. Fig. 4 shows the EBSD analysis taken from the same region on Zr-13.8Nb-0.7Hf sample at different strain. In the IQ map in bottom of Fig. 4a, the acicular BCT phases similar to those shown in Fig. 2 appear black. After 5% deformation, it can be seen from Fig. 4b that multiple intragranular bands appeared in the beta matrix after yielding. These bands are identified to be 332T according to the relationship with the beta matrix found on the stereographic projection analysis and the 51° misorientation angles across the matrix/band boundary measured in (Fig. 4c, d) respectively. From Fig.4 a and b, it can be seen that the acicular BCT phases were penetrated by twin bands after deformation. The acicular BCT phases are crossed by twins after deformation. However, the reaction of BCT phases to the twinning shear at intersection could not be analyzed due to the limited resolution of EBSD mappings.

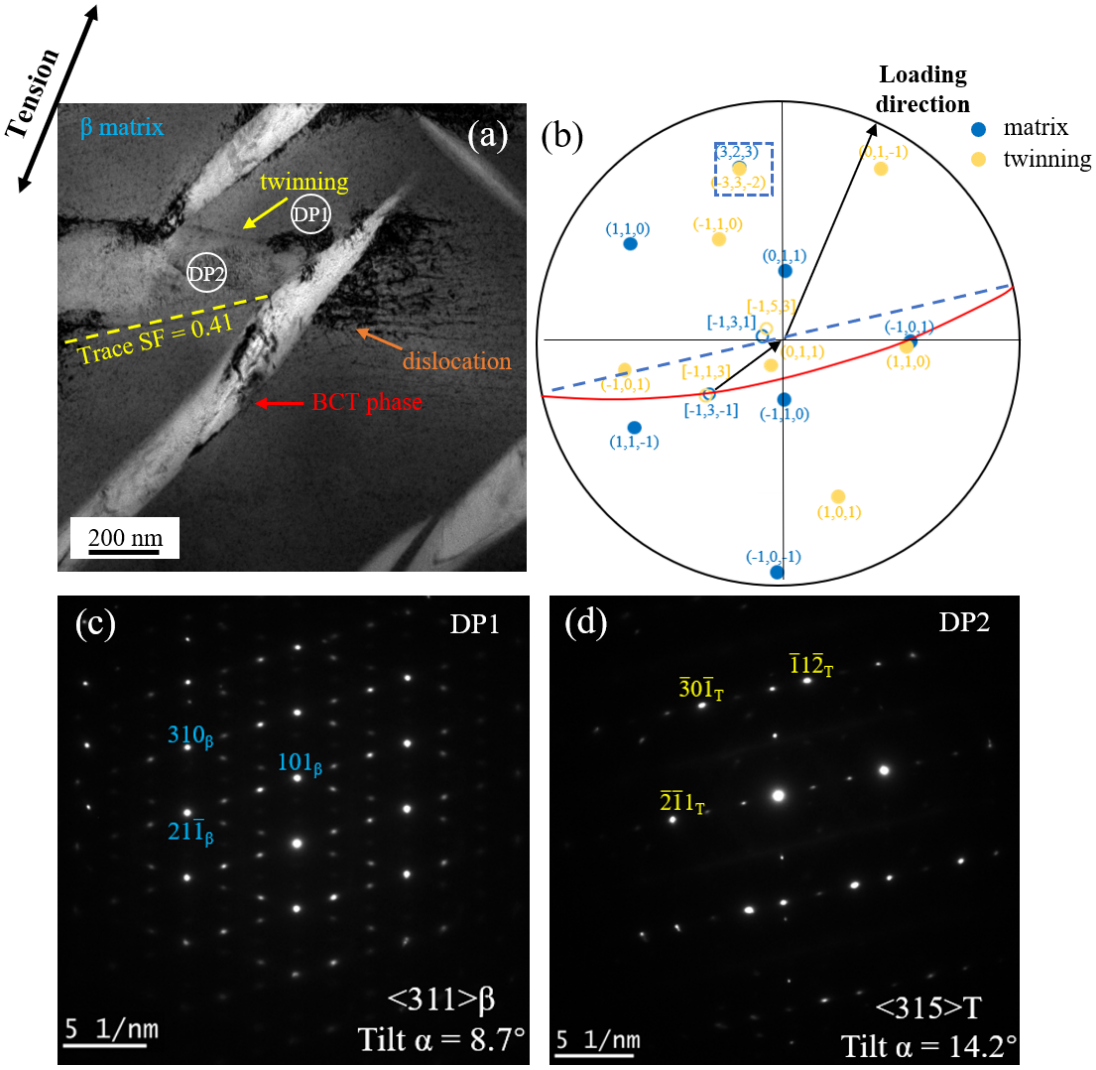

Fig. 5. *In-situ* TEM investigations of Zr-13.8Nb-0.7Hf alloy under loading. (a) BF image captured during the *in-situ* observation at the moment when the propagation of twin band (from left to right in the image) is interrupted by the BCT precipitate (the one marked by red arrow). (b) stereographic projection reconstruction of the orientation relationships (twinning plane = $(323)_{\beta}$; twinning direction = $[1\bar{3}1]_{\beta}$; Schmid factor = 0.41) between twin band and parent beta matrix. The reconstruction is performed by re-tilting the sample to different zone axes while holding the tensile strain. (c) and (d) are corresponding SAED patterns marked in (a).

To characterize the interaction between 332T and BCT precipitates, *in-situ* TEM observations were conducted in the Zr-13.8Nb-0.7Hf alloy. Fig. 5 presents the BF image and analysis of the crystallography of twin band formed during tension regarding

the tensile direction. It can be seen that the twin formed along the $(323)_\beta$ plane in $[1\bar{3}1]_\beta$ direction has a SF of 0.41, which can be ranked as the highest among all the possible twin variants in the grain. An example of strong interaction between mechanical twins and BCT precipitates is given on Fig. 5a. It can be observed that the propagation of the twin is actually strongly hindered by a BCT phase crossing in the shear plane. As observed, the propagation of the twin is efficiently blocked by the BCT precipitate. The strain misfit at the intersection seems to lead to large stress concentration at the interface between BCT phase and twinning band. The dislocation glide (orange arrow Fig. 5a) in the BCT phase following the twin shear direction is observed to accommodate the stress concentration. During the interception, no twinning in BCT was observed to accommodate the strain induced by the incoming 332T. At the opposite BCT/beta interface, a high density of dislocations could be seen, emitted into beta matrix and following the shear direction. It is worth mentioning that the 332T was fully stopped when the thickness of the BCT precipitate was close to the thickness of the TEM sample. However, in bulk sample, the 332T should be able to contour the precipitates for propagation, but still be interrupted locally before the precipitate was fully sheared by dislocation glide to reach the same strain as surrounding 332T.

Both of Zr-13.8Nb-0.7Hf and Zr-15.5Nb-0.7Hf alloys were composed of metastable beta matrix with similar grain structure and secondary quenched-in precipitates. However, the yield stress of Zr-15.5Nb-0.7Hf was much higher than that of Zr-13.8Nb-0.7Hf. The yield point in metastable alloys was controlled by the activation of deformation mechanisms at the transition from elastic to plastic regime. Similar to what was observed here, it has been reported in TRIP/TWIP Ti alloys that the yield stress increased when martensitic transformation and 332T were gradually suppressed by increasing the chemical stabilization of beta phase [27, 28] or by the presence of secondary phases [29]. According to the *in-situ* TEM observation, 332T was the primary deformation mechanism along with dislocation slip activated at yielding point in Zr-13.8Nb-0.7Hf alloy while the dislocation slip was the only deformation mechanism operated in Zr-15.5Nb-0.7Hf alloy. The higher strain-hardening rate and improved ductility of Zr-13.8Nb-0.7Hf alloy comparing to Zr-

15.5Nb-0.7Hf alloy could be attributed to the formation of 332T, resulting in the TWIP effect. When compared to the well-studied TRIP/TWIP Ti alloys [2, 4, 6, 7, 28, 30], it was observed that the strain-hardening rate in Zr-13.8Nb-0.7Hf alloy was much higher but the uniform elongation was lower. The enhanced strain-hardening effect could probably be the dynamic Hall-Petch effect resulted from the formation of twin interfaces acting as barriers to dislocation glide [31]. Such reduction of mean free path of slip, e.g. dislocation pile-ups at twin interfaces and geometrically necessary dislocations, effectively led to the increase of flow stress. Thus, higher strain-hardening rate could be attributed to the extra increase of flow stress caused by BCT which acting as obstacles to both twinning and dislocation slip. The limited uniform elongation could be probably caused by two reasons. On the one hand, the BCT acted as barriers to the multiplication, propagation and thickening of the 332T. On the other hand, the lack of micro-accommodation mechanisms such as martensite formation and hierarchical sub-twinning, highly operative in ductile TRIP/TWIP beta Ti alloy (elongation up to 45%) [2, 7, 30, 31], could be responsible to premature fracture due to local stress concentration.

In summary, the deformation mechanisms in metastable multi-phase Zr-13.8Nb-0.7Hf and Zr-15.5Nb-0.7Hf alloys have been investigated through *in-situ* SEM-EBSD and TEM microstructural characterizations. TWIP effect was observed in Zr-13.8Nb-0.7Hf alloy via 332T operation resulting in an improvement of strain-hardening rate and uniform elongation. The interaction between 332T and BCT phase was studied, showing that the secondary BCT phase could act as obstacle against twin propagation.

Declaration of Competing Interest

The authors declare that they have no known competing financial interests or personal relationships that could have appeared to influence the work reported in this paper.

Acknowledgements

Mr. Junhui TANG is sponsored by China Scholarship Council.

References

[1] D. Banerjee, J.C. Williams, Acta Mater. 61 (2013) 844-879.

[2] F. Sun, J.Y. Zhang, M. Marteleur, T. Gloriant, P. Vermaut, D. Laill´e, P. Castany, C. Curfs, P.J. Jacques, F. Prima, Acta. Mater. 61 (2013) 6406-6417.

[3] X. Min, X. Chen, S. Emura, K. Tsuchiya, Scripta Mater. 69 (2013) 393-396.

[4] F. Sun, J.Y. Zhang, M. Marteleur, C. Brozek, E.F. Rauch, M. Veron, P. Vermaut, P.J. Jacques, F. Prima, Scripta Mater. 94 (2015) 17-20.

[5] M.J. Lai, C.C. Tasan, D. Raabe, Acta Mater. 111 (2016) 173-186.

[6] M.J. Lai, T. Li, D. Raabe, Acta. Mater. 151 (2018) 67-77.

[7] B. Qian, L. Lilensten, J.Y. Zhang, M. Yang, F. Sun, P. Vermaut, F. Prima, Mater. Sci. Eng. A. 822 (2021) 141672.

[8] K. Nishimura, S. Hanada, O. Izumi, J. Mater, Sci. 25 (1990) 384-390.

[9] R. Kondo, N. Nomura, H. Doi, H. Matsumoto, Y. Tsutsumi, T. Hanawa, Mater. Trans. 57 (2016) 2060-2065.

[10] R. Kondo, N. Nomura, Suyalatu, Y. Tsutsumi, H. Doi, T. Hanawa, Acta. Biomater. 7 (2011) 4278-4284.

[11] R. Kondo, R. Shimizu, N. Nomura, H. Doi, Suyalatu, Y. Tsutsumi, K. Mitsuishi, M. Shimojo, K. Noda, T. Hanawa, Acta. Biomater. 9 (2013) 5795-5801.

[12] X.L. Zhao, L. Li, M. Niinomi, M. Nakai, D.L. Zhang, C. Suryanarayana, Acta. Biomater. 62 (2017) 372-384.

[13] B. O'Brien, W. Carroll, Acta Biomater, 5 (2009) 945-958.

[14] Suyalatu, N. Nomura, K. Oya, Y. Tanaka, R. Konda, H. Doi, Y. Tsutsumi, T. Hanawa, Acta. Biomater. 6 (2010) 1033-1038.

[15] M. Niinomi, T. Narushima, M. Nakai, Advances in Metallic Biomaterials: Tissues, Materials and Biological Reactions, in: N. Nomura (Ed.), Zirconium Alloys for Biomedical Applications, Springer, 2015, pp. 215-221.

[16] T.B. Massalski, H. Okamoto, P.R. Subramanian, L. Kacprzak, Metals Park, OH: American society for metals, 1986.

[17] F.Y. Zhou, B.L. Wang, K.J. Qiu, W.J. Lin, L. Li, Y.B. Wang, F.L. Nie, Y.F. Zheng, Mater. Sci. Eng. C. 32 (2012) 851-857.

[18] B.A. Cheadle, S.A. Aldridge, J. Nucl. Mater. 47 (1973) 255-258.

[19] M.L. Picklesimer, Oak Ridge USA Report ORNL-2422, 1957, pp.117.

[20] H.L. Yakel, Oak Ridge USA Report ORNL-2839, 1959, pp.51.

[21] M.L. Picklesimer, Oak Ridge USA Report ORNL-2839, 1959, pp.113.

[22] F. Okabe, H.Y. Kim, S. Miyazaki, Scripta. Mater. 162 (2019) 412-415.

[23] G.A. Delvecchio, D.O. Northwood, J. Rezek, J. Nucl. Mater. 35 (1970) 67-72.

[24] G.A. Delvecchio, D.O. Northwood, D.E. Osborne, J. Rezek, J. Nucl. Mater. 38 (1971) 121-131.

[25] D.O. Northwood, D.T. Lim, Can. Metall. Quart. 18 (1979) 441–467.

[26] E. Okunishi, T. Kawai, M. Mitsuhara, S. Farjami, M. Itakura, T. Hara, M. Nishida, J. Alloys Compd. 577 (2013) 713-716.

[27] B. Qian, J. Zhang, Y. Fu, F. Sun, Y. Wu, J. Cheng, P. Vermaut, F. Prima, J. Mater. Sci. Technol. 65 (2021) 228–237.

[28] J.Y. Zhang, F. Sun, Z. Chen, Y. Yang, B.L. Shen, J. Li, F. Prima, Mater. Res. Lett. 7 (2019) 251-257.
[29] F. Sun, F. Prima, T. Gloriant, Mater. Sci. Eng. A. 527 (2010) 4262–4269.
[30] J.H. Gao, Y. H. Huang, D.K. Guan, A.J. Knowles, L. Ma, D. Dye, W.M. Rainforth, Acta. Mater. 152 (2018) 301-314.
[31] L. Remy, Acta. Metall. 26 (1978) 443-451.